RSC Advances

PAPER

Cite this: *RSC Adv.*, 2022, **12**, 35452

Hollow silica-coated porous carbon with embedded iron oxide particles for effective methylene blue degradation

Kai Wang,[a] Kang Zhao, *[ab] Qingnan Meng,[ab] Qian Bai,[a] Xin Li,[a] Huating Hu,[a] Hua Jiao[ab] and Yufei Tang[ab]

Received 11th October 2022
Accepted 6th December 2022

DOI: 10.1039/d2ra06411a

rsc.li/rsc-advances

A novel catalyst, consisting of hollow silica-coated porous carbon with embedded iron oxide particles (FeO_x@C/SiO_2), was synthesized by the extended Stöber method. Iron ions were incorporated in a resorcinol–formaldehyde resin in the presence of citric acid to form a template, which was then coated with a silica layer. The iron oxide-embedded porous carbon and hollow silica were simultaneously formed during calcination under N_2 atmosphere. Through this process, silica endowed the iron oxide with low crystallinity and small size, resulting in a higher catalytic activity in the heterogeneous Fenton system for the decolorization of a methylene blue (MB) solution within 25 min. Moreover, the sample maintained 78.71% of its catalytic activity after three cycles.

1. Introduction

Water pollution has a serious impact on human health and is one of the most urgent tasks that need to be solved.[1–4] The Fenton reaction is one of the effective ways to degrade refractory organic pollutants in industrial wastewater.[5] The classical Fenton reagent consists of a homogeneous solution of iron ions and hydrogen peroxide.[6,7] However, the corresponding degradation process usually produces iron hydroxide sludge as a byproduct, causing secondary environmental pollution.[8] This has an adverse impact on the environment and limits the application scope of the catalysts. These problems can be solved using a heterogeneous Fenton catalyst.[9,10] Among these catalysts, iron oxide has attracted much attention due to its abundance, cost-effectiveness, and eco-friendliness. Xiang *et al.* reported a solvent-free preparation of α-Fe_2O_3 nanoparticles as photo-Fenton catalysts for the degradation of methyl orange.[11] Zhou *et al.* produced porous α-Fe_2O_3 rods by thermal dehydration of α-FeOOH precursors.[12] They found that α-Fe_2O_3 nanoparticles possessed more active sites for dye degradation than micrometer-sized ones. However, iron oxide nanoparticles tend to undergo to serious aggregation in the process; hence, it is essential to provide a carrier (*e.g.*, clay, carbon materials, silica, *etc.*) to ensure dispersion and efficient catalytic performance. Wang and co-workers used a reactive template method to prepare Fe_3O_4@Prussian blue core/shell composites as catalysts to enhance the degradation of RhB.[13] Under optimal conditions, the rate constant (k) of the Fe_3O_4@Prussian blue core/shell composites was ~1.5 times higher than that of Fe_3O_4 nanoclusters.

Recently, catalysts with hollow structures have attracted increasing attention, due to their large surface area and high exposure of active sites for heterogeneous Fenton reactions.[14–16] Miao *et al.* investigated the photocatalytic activity of Fe_2O_3/HPS materials calcined at different temperatures.[17] They concluded that the sample calcined at a lower temperature had higher catalytic activity, which was attributed to the lower crystallinity of iron oxide. Currently, there are two common methods to prepare hollow particles of support catalysts. The first involves the preparation of the hollow particles followed by the loading of the catalyst. Wu *et al.* used hollow silica spheres as catalyst carrier and $Fe(NO_3)_3 \cdot 9H_2O$ as iron source to obtain Fe_3O_4/SiO_2 double-mesoporous-shelled hollow spheres by solvothermal method.[18] In the second method, the preparation of the catalyst is followed by the fabrication of the hollow structure. Cheng *et al.* prepared hollow Fe_3O_4@SiO_2 microspheres by a template-etching approach.[19] This method consisted of four steps: preparation of Fe_2O_3, coating with the SiO_2 shell, etching, and heating in reducing atmosphere. However, both methods are time-consuming, which hinders their wide application.

In light of the above findings, hollow particles of the supported catalyst were prepared by a one-pot method. We prepared hollow silica-coated porous carbon embedded with iron oxide (FeO_x@C/SiO_2) composites by an extended Stöber method. During the annealing process, iron oxide-intercalated porous carbon and hollow silica were obtained simultaneously. In addition, silica promoted the formation of iron oxide particles with low crystallinity and small size, and the resulting composite exhibited superior performance in the

[a]*Department of Materials Science and Engineering, Xi'an University of Technology, Xi'an 710048, PR China. E-mail: kzhao@xaut.edu.cn*

[b]*Shaanxi Province Key Laboratory of Corrosion and Protection, Xi'an University of Technology, Xi'an 710048, PR China*

degradation of methylene blue (MB) than the FeO_x@C counterpart.

2. Experimental

2.1. Material

All chemicals were of analytical reagent grade and used without purification. $FeCl_3 \cdot 6H_2O$, $NH_3 \cdot H_2O$ (25%), H_2O_2 (30%), citric acid monohydrate ($C_6H_8O_7 \cdot H_2O$), resorcinol ($C_6H_4(OH)_2$), tetraethoxysilane ($Si(OC_2H_5)_4$), formaldehyde (HCHO), and ethanol (C_2H_5OH) were obtained from Sinopharm Chemical Reagent Company.

2.2. Synthesis of FeO_x@C/SiO_2 hollow nanoparticles

The FeO_x@C/SiO_2 hollow nanoparticles were synthesized by a one-pot two-step method. First, 0.5 mM $FeCl_3 \cdot 6H_2O$ and 71.4 mg $C_6H_8O_7 \cdot H_2O$ were added to a mixture solution of 15 mL H_2O and 12 mL C_2H_5OH, stirring until complete dissolution, respectively. Next, 0.8 mL $NH_3 \cdot H_2O$, 0.2 g $C_6H_4(OH)_2$, and 0.28 mL HCHO were sequentially added to the above solution to synthesize Fe-RF nanoparticles by stirring for 10 h. Finally, the silica shell was prepared by adding 40 mL C_2H_5OH, 0.8 mL $NH_3 \cdot H_2O$, and 0.75 mL $Si(OC_2H_5)_4$, followed by stirring overnight. The precipitates formed in the solution were collected by centrifugation and denoted as Fe-RF@SiO_2. The final FeO_x@C/SiO_2 samples (denoted as 0.5-FCS-500) were obtained by annealing for 2 h at 500 °C in N_2 atmosphere. The products prepared by adding 1.0 mM and 1.5 mM $FeCl_3 \cdot 6H_2O$ were labeled 1.0-FCS-500 and 1.5-FCS-500, respectively. For comparison, pure FeO_x@C nanoparticles (1.0-FC-500) were also prepared by direct calcination of Fe-RF nanoparticles.

2.3. Characterization

The crystal structure of FeO_x@C/SiO_2 was determined by X-ray diffraction (XRD, Bruker D8) with Cu K_α radiation at 40 kV and 40 mA. The measurements were carried out in the 2θ range of 20–80° with a scanning step of 8° min^{-1}. Thermogravimetric analysis (TGA, DTG-60AH) was performed to monitor the pyrolysis carbonization process of the sample. Under N_2 atmosphere, the TG curve was obtained in the temperature range of 30–1000 °C at a rate of 10 °C min^{-1}. Fourier transform infrared (FTIR) spectroscopy (Nicolet Avatar 360) was used to identify the molecular vibration modes; the measurements were carried out by the KBr method in the range of 4000 to 400 cm^{-1}. The morphology of the samples was inspected by scanning electron microscopy (SEM, JSM-6700F). The inner structure of the nanoparticles was examined by transmission electron microscopy (TEM, JEM-3010). In addition, the average diameter size was averaged over 100 nanoparticles. The specific surface area and pore structure of the samples were analyzed by N_2 adsorption–desorption at 77 K using an ASAP 2020 system. In the test, 250 mg of the samples were kept at the degassing temperature of 200 °C for 10 h. X-ray photoelectron spectroscopy (XPS, Thermo Scientific K-Alpha) was used to determine the valence states of the elements. High-resolution spectra were recorded using a monochromatic 150 W Al K_α radiation source and a pass energy of 50 eV. Binding energies were referenced to the standard C 1s signal at 284.80 eV. The amount of iron in solution was determined by inductively coupled plasma-atomic emission spectroscopy (ICP-AES), using an ICAP 6500 Thermo Scientific device. The catalytic degradation of MB was monitored with a 7600 MC UV-Vis spectrophotometer (BILON).

2.4. Catalytic activity

The heterogeneous Fenton catalytic activities of hollow FeO_x@C/SiO_2 were evaluated by studying the catalytic degradation of MB. Typically, 15 mg of catalyst was poured into a 100 mL MB solution ($c_0 = 0.1$ mM, pH = 3, $T = 30$ °C) under magnetic stirring. Afterward, the mixed solution was stirred for 30 min to reach the adsorption–desorption equilibrium, followed by the addition of 60 μL H_2O_2. At intervals of 3 min, 1 mL solution aliquots were extracted and filtered through a membrane (0.22 μm). The concentration of MB was determined based on the absorption intensity at 664 nm, as follows:

$$\text{Degradation rate} = C/C_0$$

where C and C_0 denote the dye concentration at a certain time and its initial value, respectively.

To evaluate the stability of the catalyst, the nanoparticles were collected from the mixed solution by centrifugation, washed with deionized water, and then redispersed into fresh MB solution for the next cycle. In the iron ion leaching experiment, the solution obtained after centrifugation was directly used for ICP measurements.

Free radical elimination tests were performed under the same conditions as the catalytic experiments. When the catalyst reached the adsorption–desorption equilibrium, H_2O_2 and a scavenger [*tert*-butyl alcohol (TBA) or *p*-benzoquinone (BQ)] were added at the same time, and then 1 mL solution aliquots were collected at intervals of 3 min for testing.

3. Results and discussion

Fig. 1a shows the pyrolysis process of Fe-RF@SiO_2. The first stage (25–200 °C) corresponded to a weight loss of 12%, which was attributed to the evaporation of adsorbed water and the evolution of unreacted oligomers.[20] The second weight loss stage (24%) in the range of 200–800 °C was ascribed to the formation of FeO_x and carbonization of Fe-RF during pyrolysis.[21] In the final stage (800–900 °C), the weight loss was due to the structural ordering of the carbon matrix. The TG curve of Fe-RF (Fig. 1b) also included three processes: evaporation of adsorbed water (25–200 °C), carbonization of Fe-RF (200–600 °C), and ordering of carbon atoms (600–900 °C). Compared with Fe-RF@SiO_2, the FeO_x formation temperature of Fe-RF was lower, which was attributed to the silica shell preventing grain growth.

The XRD patterns of 1.0-FCS-500 samples prepared at different temperatures are shown in Fig. 2a. No distinct diffraction peaks were observed in the curves after pyrolysis at 400 and 500 °C, indicating that the FeO_x particles embedded in silica were either in amorphous form or of a size too small to be detected by X-ray diffraction. When the temperature increased

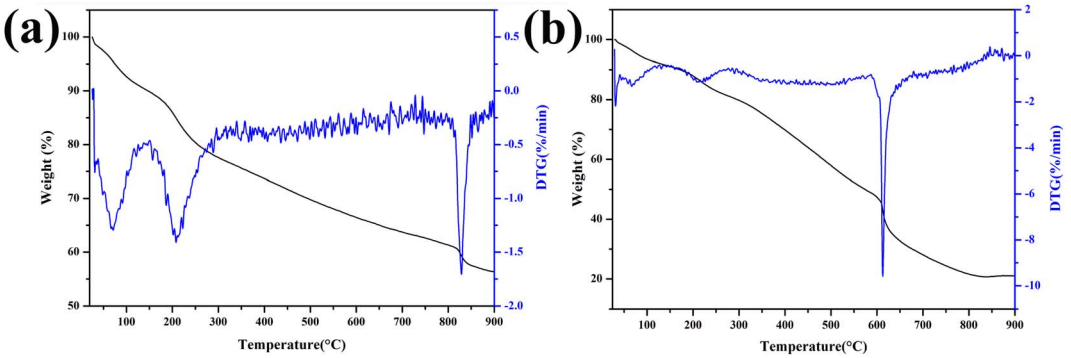

Fig. 1 TG curves of Fe-RF@SiO_2 (a) and Fe-RF (b).

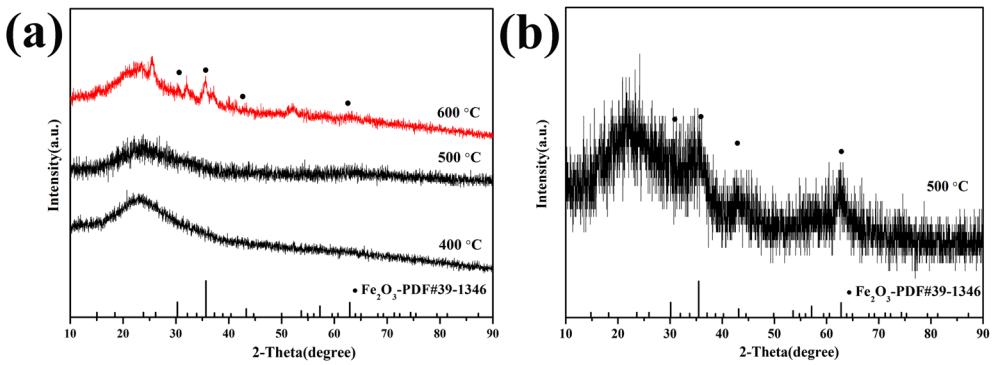

Fig. 2 XRD patterns of 1.0-FCS-500 (a) and 1.0-FC-500 (b) samples prepared at different temperatures.

to 600 °C, four peaks appeared at $2\theta = 30.2°$, 35.6°, 43.2°, and 62.9°, corresponding to the (220), (311), (400), and (440) crystal faces of Fe_2O_3 (PDF #39-1346),[22] respectively. These results show that increasing the temperature is beneficial to grain growth. For comparison, 1.0-FC-500 also exhibited four peaks corresponding to Fe_2O_3 (Fig. 2b). This demonstrates that the silica shell layer can effectively prevent the crystallization of grains.[23] A higher temperature is believed to favor the formation of stable carbon structures by resorcinol–formaldehyde pyrolysis. Therefore, to achieve a lower crystallinity and stable porous carbon structure of the products, the Fe-RF@SiO_2 samples were calcined at 500 °C to prepare 1.0-FCS-500.

The iron content and valence state of the samples prepared with different dosages were analyzed by XPS, as shown in Fig. 3. As shown in the high-resolution Fe 2p XPS spectrum (Fig. 3a), two peaks at 710.44 and 724.16 eV were attributed to the Fe $2p_{3/2}$ and Fe $2p_{1/2}$ states of Fe(II), respectively. In addition, the two peaks at 711.77 and 726.41 eV were attributed to Fe(III) Fe $2p_{3/2}$ and Fe $2p_{1/2}$ signals, respectively.[24,25] The Fe $2p_{3/2}$ and Fe $2p_{1/2}$ signals did not shift with increasing Fe content (Fig. 3b and c). Table 1 shows that the iron content of the final sample increased with increasing $FeCl_3 \cdot 6H_2O$ content. When the added amount of $FeCl_3 \cdot 6H_2O$ was 1.0 mM, the Fe(II) content was the highest, which was beneficial for the Fenton reaction.[26]

The chemical structure of 1.0-FCS-500 was analyzed by FTIR spectroscopy. The spectrum in Fig. 4 shows a broad band at 3463 cm^{-1}, corresponding to the –OH groups of surface water molecules. The peaks located at 1088, 794, and 467 cm^{-1} were attributed to asymmetric and symmetric stretching vibrations of Si–O–Si bonds and bending vibrations of Si–O bonds, respectively.[27] These results confirmed the presence of SiO_2 in the sample. The peak at 562 cm^{-1} was assigned to Fe–O flexural vibrations, indicating the successful formation of FeO_x.[28] The bands at 1088 and 1637 cm^{-1} were attributed to C–O–C stretching and aromatic ring vibrations, respectively. The band at 1579 cm^{-1} confirmed the presence of C=C bonds, corresponding to the normal stretching of carbonaceous molecules. Moreover, the peak at 1407 cm^{-1} was assigned to C–C bond vibrations, related to the carbonaceous structure of the composites. In the spectrum of 1.0-FC-500, two distinct peaks appeared at 3463 and 1597 cm^{-1}, corresponding to the absorptions of –OH and C=C groups, respectively. In addition, the spectrum displayed an absorption peak corresponding to Fe–O bonds at 562 cm^{-1}, but no SiO_2 absorption peaks.

Fig. 5 shows the morphology and structure of 1.0-FCS-500. The sample displayed uniform cavity and a worm-like morphology, implying the successful production of a hollow structure (Fig. 5a and b). The shell thickness was 9.9 ± 1.1 nm, depending on the amount of tetraethoxysilane added. The diameters of the inner cavity and of the nanoparticles embedded in the shell formed simultaneously during the calcination process, were approximately 18.4 ± 3.1 and 2.2 ± 0.5 nm, respectively. The corresponding SEM images show an irregular morphology, which was attributed to the interaction

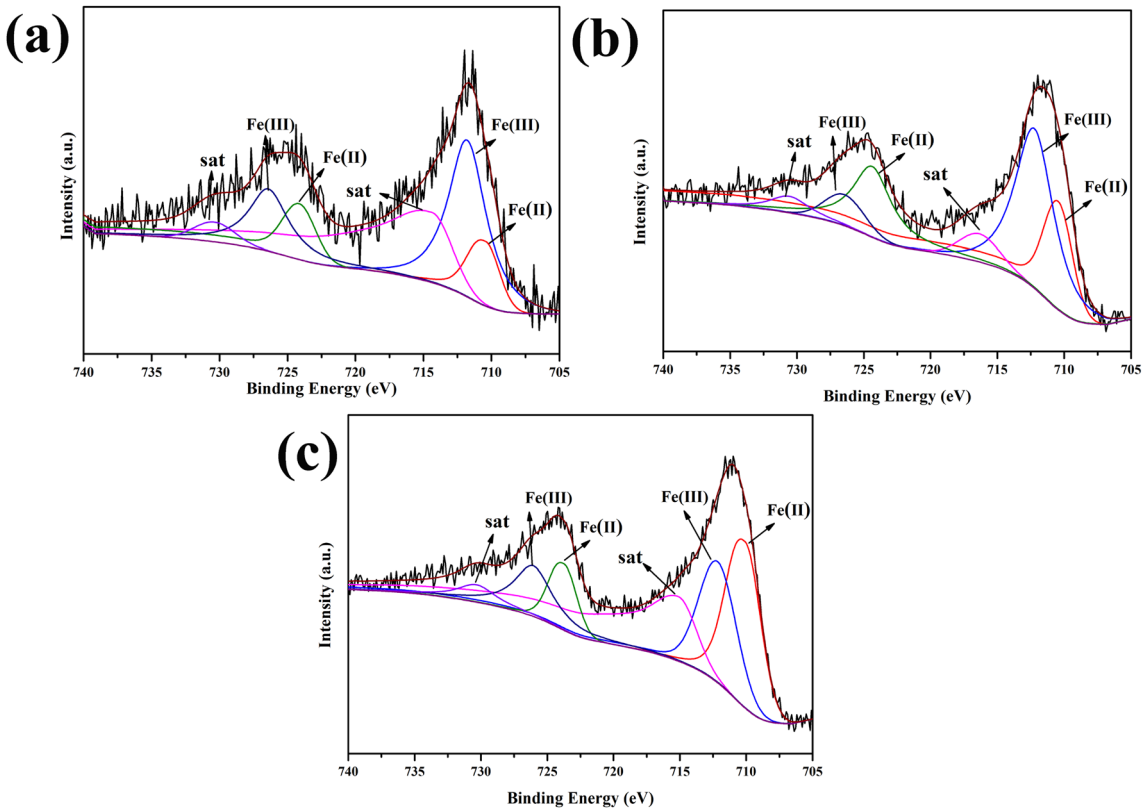

Fig. 3 XPS spectra of 0.5-FCS-500 (a), 1.0-FCS-500 (b), and 1.5-FCS-500 (c).

Table 1 Elemental composition of different samples

Sample	Fe (Fe(II)/Fe)/at%	C/at%	O/at%	Si/at%
0.5-FCS-500	1.09 (32.95%)	16.73	54.06	28.11
1.0-FCS-500	1.74 (54.09%)	12.05	57.98	28.22
1.5-FCS-500	2.1 (50.21%)	11.88	58.64	27.38

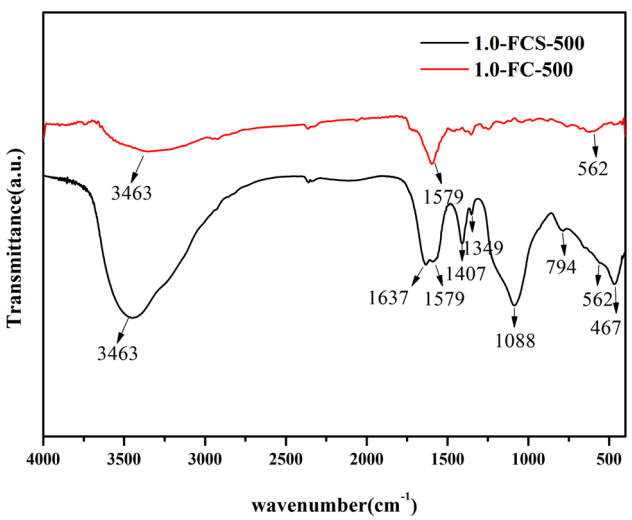

Fig. 4 FTIR spectra of 1.0-FCS-500 and 1.0-FC-500 samples.

between Fe^{3+} and the resorcinol–formaldehyde resin to form a worm-like template under the action of citric acid (Fig. 5c and d). The energy-dispersive spectroscopy (EDS) mapping images of 1.0-FCS-500 (Fig. 5e–i) show that the Fe/Si/C/O elements were evenly distributed in the samples, indicating their good dispersion, which is beneficial for MB degradation.

The TEM images are shown in Fig. 6a and b. In all cases, many nanoparticles were uniformly dispersed over the porous carbon support and no agglomerates were detected. The mean particle size of the nanoparticles was approximately 4.8 nm, which was slightly larger than that of the 1.0-FCS-500 particles. These data confirm that the silica shell prevented the grain growth and crystallization.[18,21] Finally, 1.0-FC-500 exhibited an irregular morphology, similar to that of 1.0-FCS-500 (Fig. 6c and d).

Fig. 7 shows the TEM images of 1.0-FCS-500 after NaOH etching. As shown in the figure, the core–shell structure of the sample disappeared, resulting in a uniform worm-like porous structure. Compared with the 1.0-FCS-500 sample before etching, the sample showed a roughened surface, indicating that the SiO_2 shell was completely etched. Moreover, the hollow structure was also destroyed, which was attributed to the low strength of porous carbon. These results indicate that 1.0-FCS-500 contained silica and carbon in its hollow structure, which is beneficial for organic dye degradation.[29]

The N_2 adsorption–desorption isotherms of 1.0-FCS-500 and 1.0-FC-500 are shown in Fig. 8; both samples showed type IV isotherms. The hysteresis loops (type H3) in the isotherms

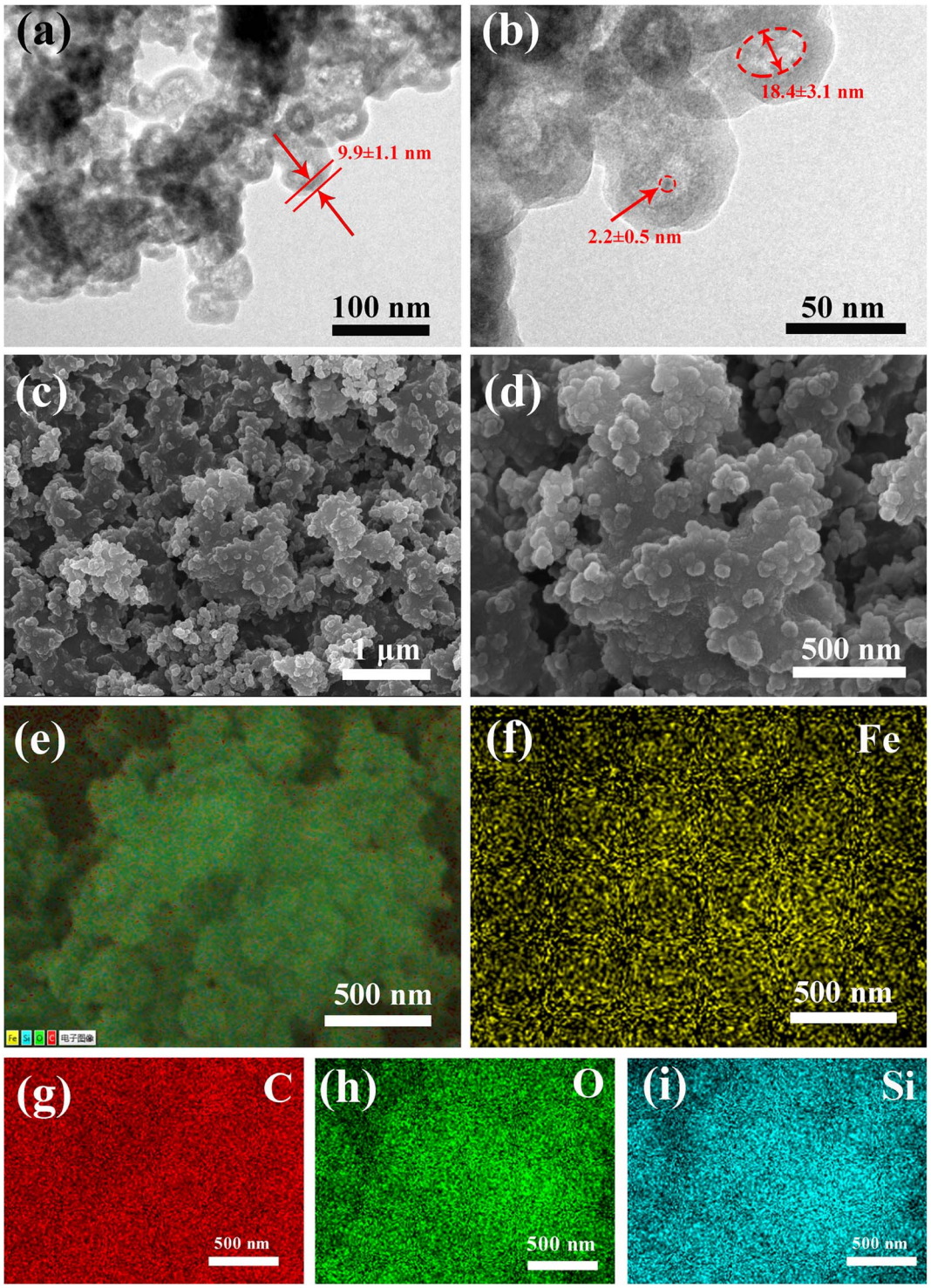

Fig. 5 TEM (a and b), SEM (c and d), and EDS (e–i) images of 1.0-FCS-500.

suggest the presence of mesopores in both materials.[30] The Brunauer–Emmett–Teller (BET) surface areas of 1.0-FCS-500 and 1.0-FC-500 were 191.03 and 306.53 $m^2\ g^{-1}$, respectively. The corresponding pore size distributions were estimated using Barrett–Joyner–Halenda (BJH) analysis (Fig. 8b).

Fig. 9a shows the degradation efficiency of catalysts with different iron contents. The degradation efficiency of the catalyst prepared with 0.5 mM $FeCl_3 \cdot 6H_2O$ fluctuated around a constant value. As the $FeCl_3 \cdot 6H_2O$ content increased to 1.0 mM, the degradation rate reached 100% in 25 min, indicating that increasing the iron content can significantly improve the degradation efficiency. Upon continuing to increase the $FeCl_3 \cdot 6H_2O$ content to 1.5 mM, the time required for the complete MB degradation was the same as that of the

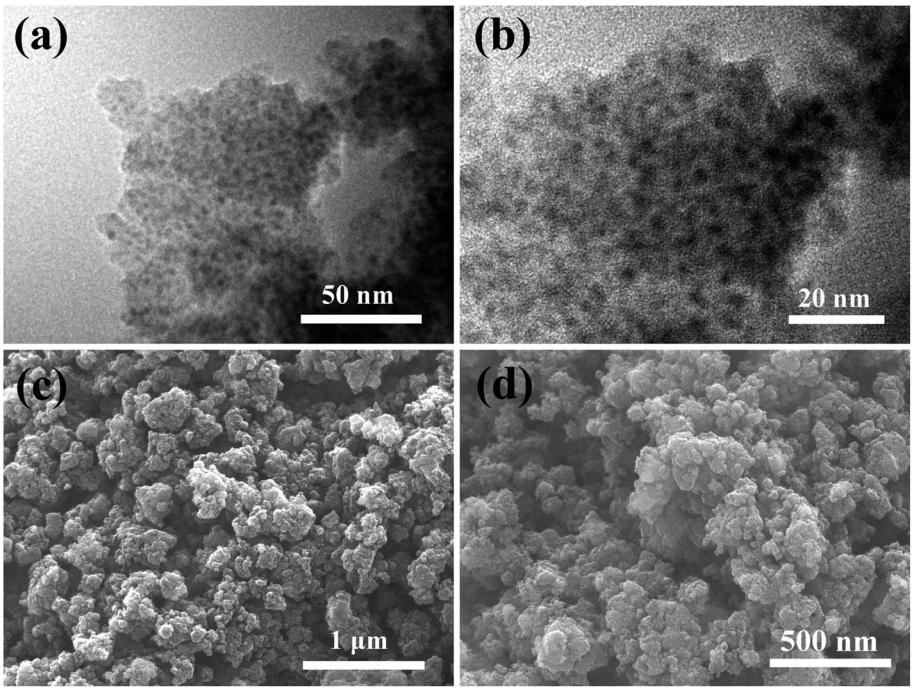

Fig. 6 TEM (a and b) and SEM (c and d) images of 1.0-FC-500.

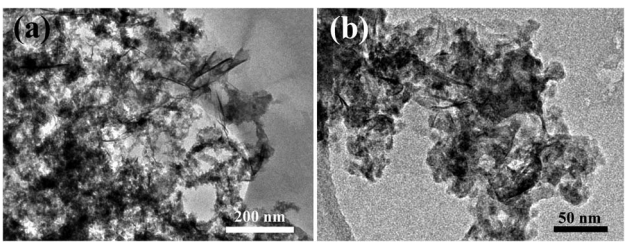

Fig. 7 TEM images of 1.0-FCS-500 after NaOH etching (a) low magnification (b) high magnification.

sample with 1.0 mM content. Based on their combination of economy and degradation efficiency, the samples prepared with 1.0 mM content were selected for further characterization after pyrolysis at different temperatures. After pyrolysis at 400 °C, the degradation efficiency of the product was reduced to 55%, which was attributed to its low specific surface area, providing fewer reaction sites. However, when the temperature increased to 600 °C, the degradation efficiency remained almost constant, due to the higher crystallinity. To study the catalytic mechanism, Fig. 9b shows the degradation efficiency evaluated in comparative experiments. In the absence of H_2O_2, 1.0-FCS-500 only exhibited adsorption capacity. In contrast, in absence of 1.0-FCS-500, the MB solution remained stable upon adding H_2O_2. Moreover, the degradation rate of 1.0-FC-500 fluctuated around a constant value, likely due to the higher crystallinity and larger size of FeO_x nanoparticles, leading to fewer and less active Fe ions exposed on the surface.[19,21] Fig. 9c shows the first-order kinetic model for MB degradation under different conditions. The MB degradation rate constants of 1.0-FCS-500 and 1.0-FC-500 were 0.11507 ± 0.01396 and 0.00127 ±

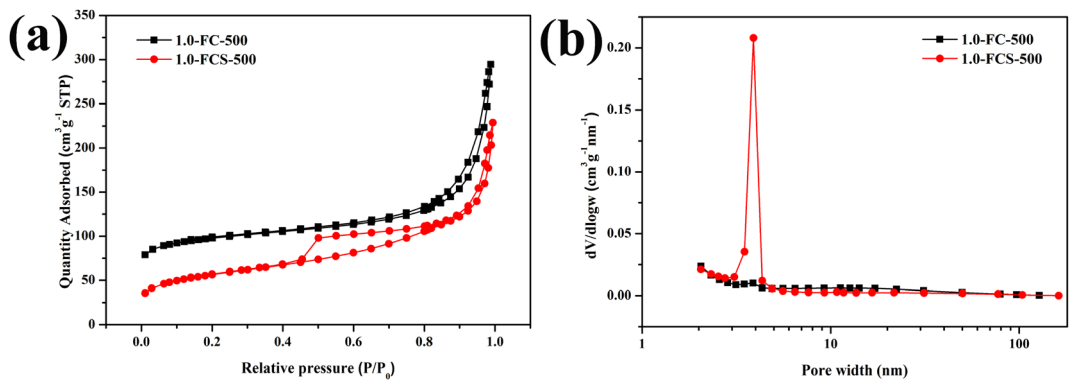

Fig. 8 N_2 adsorption–desorption isotherms (a) and pore size distributions (b) of 1.0-FCS-500 and 1.0-FC-500.

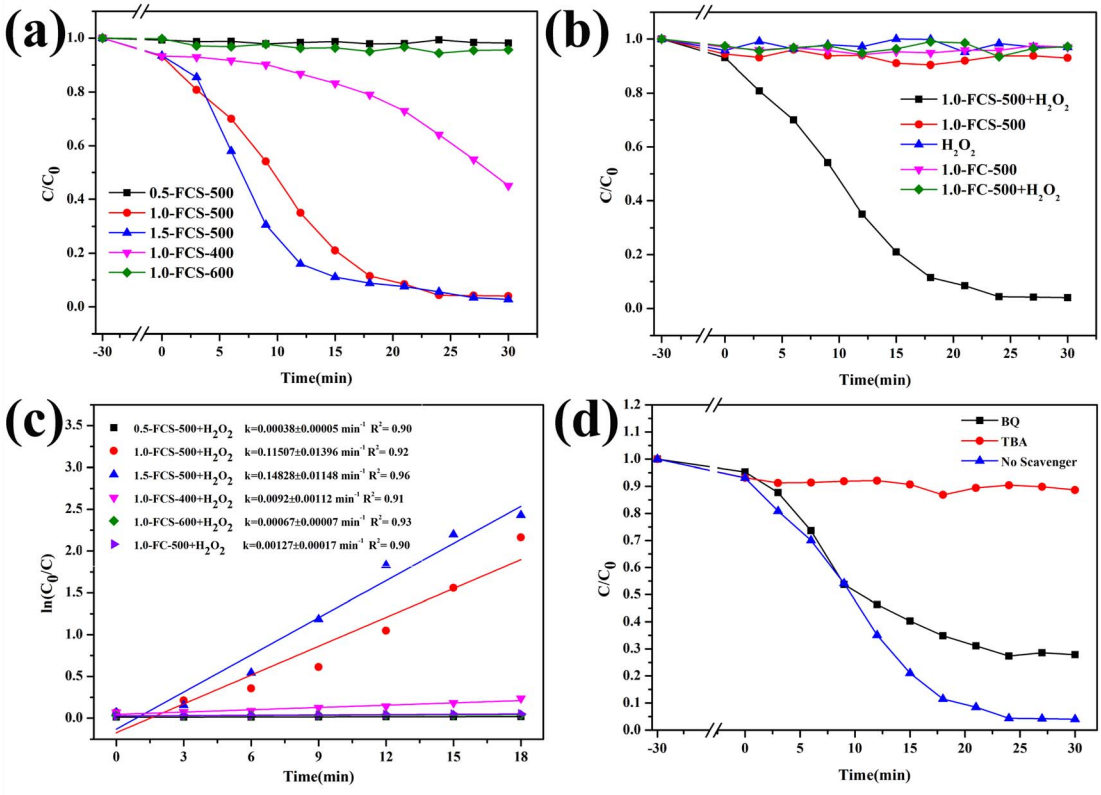

Fig. 9 Removal efficiency of MB (a, b and d) and $\ln(C_0/C)$ *vs.* reaction time plots (c) under different conditions.

0.00017 min^{-1}, respectively. Compared with other studies, 1.0-FCS-500 showed a superior MB degradation ability (see comparison in Table 2). Free radical scavenging experiments were employed to explore the radical species produced by degradation. In particular, TBA and BQ were used to scavenge hydroxyl radicals (·OH) and superoxide ($O_2^{\bullet-}$) radicals, respectively. Compared to the reaction without scavenger, the MB degradation efficiency was slightly reduced with the addition of BQ (Fig. 9d).[31] In the presence of TBA, the MB degradation efficiency was significantly reduced, indicating that ·OH was the main active species for MB degradation.

The stability and reusability of 1.0-FCS-500 were investigated by recycling reactions under the same conditions (Fig. 10a). We found that the degradation rate of 1.0-FCS-500 only decreased from 95.16% to 92.07% after two cycles, mainly attributed to the loss of small-sized iron ions under acidic conditions. In the third cycle, the MB degradation rate was only 78.71%, but the iron ion concentration was 0.85 mg mL^{-1}, which was lower than that of the two previous cycles. The second reason could be that there are fewer activation sites, due to the coverage area of the intermediate products. The Fe 2p XPS spectrum of 1.0-FCS-500 after three cycles is shown in Fig. 10b. The Fe $2p_{3/2}$ and Fe $2p_{1/2}$ peaks were located at 711.9 and 725.1 eV, respectively; these values were consistent with the binding energies of the fresh sample. According to the fitting results, the atomic ratio of Fe(III) increased from 45.91% to 63.76%, indicating that the

Table 2 Comparison of catalytic performances of various Fe-based catalysts

	Catalyst	Catalyst dosage	H_2O_2 dosage	Organic species	Degradation time and rate	Reference
1	Fe_2O_3/TiO_2-BC	0.2 g L^{-1}	2 mL (H_2O_2)	20 mL, 50 mg L^{-1} MB	60 min/100%	32
2	Mesoporous $Fe_2O_3 \cdot SiO_2$	0.5 g L^{-1}	12 mM (H_2O_2)	100 mL, 50 mg L^{-1} tartrazine	80 min/98.5%	33
3	MIL100(Fe)/GO	0.5 g L^{-1}	8 mM (H_2O_2)	40 mL, 50 mg L^{-1} MO	80 min/98%	34
4	Mesoporous Fe_2O_3–SiO_2	2.0 g L^{-1}	2 mL (H_2O_2)	10 mL, 0.6 g L^{-1} MO	20 min/98.5%	35
5	Fe_2O_3@mesoSiO$_2$	0.5 g L^{-1}	9.0 g L^{-1} (H_2O_2)	50 mg L^{-1} MB	120 min/99%	36
6	Fe_2O_3@mesoSiO$_2$	0.5 g L^{-1}	18 g L^{-1} (H_2O_2)	50 mg L^{-1} MB	400 min/90%	37
7	FeO_x@GC-NBC	0.06 g L^{-1}	1 mM PDS	2 mg L^{-1} BPA	30 min/100%	38
8	FeO_x@g-BC	0.2 g L^{-1}	0.5 mL (H_2O_2)	100 mL, 20 mg L^{-1} TC	15–60 min/100%	39
9	Fe_3O_4–Cs	0.5 g L^{-1}	10 mM H_2O_2	0.1 mM TC	20 min/96.2%	40
10	FeO_x/SiO_2	10.0 g L^{-1}	2 mL H_2O_2	50 mL, 1 g L^{-1} MB	72 h/99.94%	41
11	1.0-FCS-500	0.15 g L^{-1}	60 μL (H_2O_2)	100 mL, 37.3 mg L^{-1} MB	30 min/100%	This work

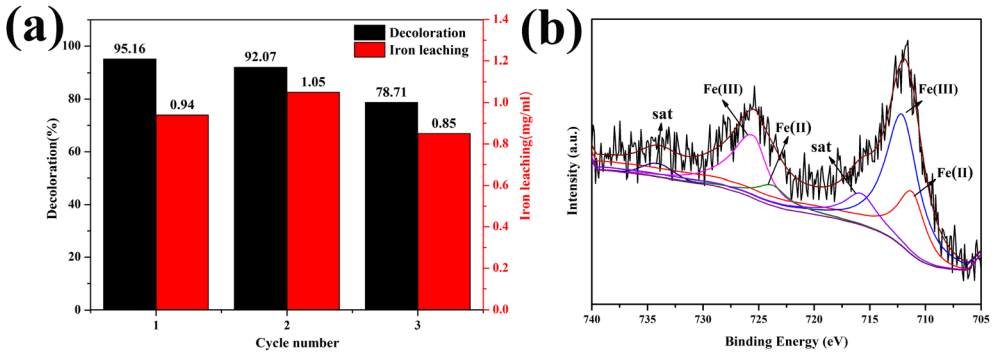

Fig. 10 (a) Recycling performance and (b) Fe 2p XPS spectrum of 1.0-FCS-500 after three cycles.

surface Fe(II) species were only slightly oxidized.[42] In conclusion, the 1.0-FCS-500 catalyst possessed good stability and recyclability.

4. Conclusion

In this study, a novel catalyst (1.0-FCS-500) was synthesized by the extended Stöber method. Structural analysis indicated that hollow-structure and small-sized FeO_x particles were located within the silica shell. Compared to 1.0-FC-500, the iron oxide particles in 1.0-FCS-500 had lower crystallinity and smaller size. MB was almost completely degraded by 1.0-FCS-500 within 25 min, with a degradation rate constant of 0.11507 ± 0.01396 min^{-1}. Free radical scavenging experiments showed that ·OH radicals were the main active species for MB degradation. After three cycles, the catalytic degradation rate gradually decreased to 78.71%, mainly due to the leaching of Fe ions.

Conflicts of interest

The authors declare that they have no conflict of interest.

Acknowledgements

The research was financially supported by the National Natural Science Foundation of China (No. 52172074) and the Doctoral Innovation Fund of Xi'an University of Technology (No. 310-252072005).

References

1 K. A. M. Ahmed, H. Peng, K. B. Wu and K. X. Huang, *Chem. Eng. J.*, 2011, **172**, 531–539.
2 M. Z. Shahid, L. Yu and R. Mehmood, *Catal. Sci. Technol.*, 2020, **10**, 2242–2253.
3 M. Z. Shahid, R. Mehmood, M. Athar, J. Hussain, Y. W. Wei and A. Khaliq, *ACS Appl. Nano Mater.*, 2021, **4**, 746–758.
4 M. Z. Shahid, R. Mehmood, U. Farooq and F. P. Han, *Adv. Powder Technol.*, 2020, **31**, 1708–1719.
5 M. N. Han, X. G. Duan, G. L. Cao, S. S. Zhu and S. H. Ho, *Process Saf. Environ. Prot.*, 2020, **139**, 230–240.
6 S. R. Pouran, A. R. A. Aziz and W. M. A. W. Daud, *J. Ind. Eng. Chem.*, 2015, **21**, 53–69.
7 M. Punzi, B. Mattiasson and M. Jonstrup, *J. Photochem. Photobiol., A*, 2012, **248**, 30–35.
8 A. Babuponnusami and K. Muthukumar, *J. Environ. Chem. Eng.*, 2014, **2**, 557–572.
9 Q. N. Meng, L. L. Du, J. Yang, Y. F. Tang, Z. H. Han, K. Zhao and G. J. Zhang, *Colloids Surf., A*, 2018, **548**, 142–149.
10 M. E. Hassan, Y. B. Chen, G. L. Liu, D. W. Zhu and J. B. Cai, *J. Water Process. Eng.*, 2016, **12**, 52–57.
11 H. L. Xiang, G. K. Ren, X. S. Yang, D. H. Xu, Z. Y. Zhang and X. L. Wang, *Ecotoxicol. Environ. Saf.*, 2020, **200**, 110744.
12 X. M. Zhou, H. C. Yang, C. X. Wang, X. B. Mao, Y. S. Wang, Y. L. Yang and G. Liu, *J. Phys. Chem. C*, 2010, **114**, 17051–17061.
13 Q. Q. Wang, Y. Yang, S. C. Ma, J. Wu and T. J. Yao, *Colloids Surf., A*, 2020, **606**, 125416.
14 H. F. Zhou, J. Yang, W. Cao, C. Chen, C. Y. Jiang and Y. P. Wang, *Appl. Surf. Sci.*, 2022, **590**, 153120.
15 R. R. Ding, W. Q. Li, C. S. He, Y. R. Wang, X. C. Liu, G. N. Zhou and Y. Mu, *Appl. Catal., B*, 2021, **291**, 120069.
16 Y. N. Guan, G. Fu, Q. Q. Wang, S. C. Ma, Y. Yang, B. F. Xin, J. X. Zhang, J. Wu and T. J. Yao, *Sep. Purif. Technol.*, 2022, **299**, 121699.
17 Z. H. Miao, S. Y. Tao, Y. C. Wang, Y. X. Yu, C. G. Meng and Y. L. An, *Microporous Mesoporous Mater.*, 2013, **176**, 178–185.
18 X. P. Wu and Z. D. Nan, *Mater. Chem. Phys.*, 2019, **227**, 302–312.
19 L. Cheng, Y. Y. Liu, B. F. Zou, Y. Yu, W. M. Ruan and Y. Q. Wang, *Mater. Sci. Eng., C*, 2017, **75**, 829–835.
20 Q. N. Meng, K. Wang, X. B. Xu, Y. F. Tang, Z. H. Han, K. Zhao, G. J. Zhang, J. N. Cui and Y. Y. Ji, *ChemistrySelect*, 2018, **3**, 8919–8925.
21 Q. N. Meng, K. Wang, Y. F. Tang, K. Zhao, G. J. Zhang and L. Zhao, *J. Alloys Compd.*, 2017, **722**, 8–16.
22 X. Y. Hou, J. L. Kang, G. Zhou and J. T. Wang, *Mater. Lett.*, 2022, **313**, 131736.
23 K. Wang, Q. N Meng, L. L. Du, Y. F. Tang and K. Zhao, *J. Nanopart. Res.*, 2021, **23**, 27.
24 W. L. Zhao, Y. Fu, Y. Chen, J. Sun, Q. Tang, B. H. Jiang, H. H. Kong, F. Xu and Q. M. Ji, *Microporous Mesoporous Mater.*, 2021, **312**, 110704.

25 J. C. Wang, B. B. Wang, W. N. Shi, X. Qiao, X. X. Yang, L. F. Zhang, W. Q. Zhang, R. L. Li and Y. X. Hou, *J. Environ. Chem. Eng.*, 2022, **10**, 108565.
26 S. L. Orozco, E. R. Bandala, C. A. Arancibia-Bulnes, B. Serrano, R. Suárez-Parra and I. Hernández-Pérez, *J. Photochem. Photobiol., A*, 2008, **198**, 144–149.
27 Q. N. Meng, S. Y. Xiang, W. Cheng, Q. N. Chen, P. F. Xue, K. Zhang, H. C. Sun and B. Yang, *J. Colloid Interface Sci.*, 2013, **405**, 28–34.
28 S. Pirsa and F. Asadzadeh, *Adv. Powder Technol.*, 2021, **32**, 1233–1246.
29 Q. N. Meng, K. Wang, Y. F. Tang, K. Zhao, G. J. Zhang, Z. H. Han and J. Yang, *ChemistrySelect*, 2017, **2**, 10442–10448.
30 Q. N. Meng, J. N. Cui, K. Wang, Y. F. Tang, K. Zhao and L. Huang, *Mol. Catal.*, 2020, **493**, 111107.
31 Z. W. Xie, J. Yang, K. Wang, Q. N Meng, Y. F. Tang and K. Zhao, *Ceram. Int.*, 2022, **48**, 9114–9123.
32 X. L. Chen, F. Li, H. Y. Chen, H. J. Wang and G. G. Li, *J. Environ. Chem. Eng.*, 2020, **8**, 103905.
33 A. T. Vu, T. N. Xuan and C. H. Lee, *J. Water Process. Eng.*, 2019, **28**, 169–180.
34 J. T. Tang and J. L. Wang, *RSC Adv.*, 2017, **7**, 50829.
35 N. Panda, H. Sahoo and S. Mohapatra, *J. Hazard. Mater.*, 2011, **185**, 359–365.
36 Z. M. Cui, J. Hao, J. Liu and W. G. Song, *RSC Adv.*, 2016, **6**, 74545–74549.
37 Z. M. Cui, Z. Chen, C. Y. Cao, L. Jiang and W. G. Song, *Chem. Commun.*, 2013, **49**, 2332.
38 Y. J. Wang, L. Wang, F. Ma and Y. Q. You, *Chem. Eng. J.*, 2022, **438**, 135552.
39 X. Zhang, H. Y. Wu, M. Chen and Z. L. Li, *Int. J. Biol. Macromol.*, 2022, **205**, 329–340.
40 X. Y. Li, K. P. Cui, Z. Guo, T. T. Yang, Y. Cao, Y. P. Xiang, H. H. Chen and M. F. Xi, *Chem. Eng. J.*, 2020, **379**, 122324.
41 L. Liu, S. Q. Liu, S. B. Mishra and L. P. Sheng, *Ceram. Int.*, 2019, **45**, 15475–15481.
42 D. B. Jiang, X. Y. Liu, X. Xu and Y. X. Zhang, *J. Phys. Chem. Solids*, 2018, **112**, 209–215.